

Soil-Geogrid Interaction Analysis Using A Coupled Finite-Discrete Element Method



Viet D.H. Tran, Mohamed A. Meguid & Luc E. Chouinard
Department of Civil Engineering-McGill University, Montreal, QC, Canada

ABSTRACT

The response of geogrid reinforcement is mainly dependent on the interaction between the geogrid and surrounding soil. Modeling this interaction is challenging, particularly, if details are needed at the particle scale level. A new numerical framework that takes advantage of both the finite and discrete element approaches to investigate soil-geogrid interaction problems is described in this paper. The proposed method uses finite elements to model the geogrid and discrete particles to model the surrounding soil to reflect the discontinuous nature of the granular material. The coupled framework is used to simulate two geotechnical problems, namely, geogrid pullout test and strip footing on geogrid-reinforced sand. The numerical results are validated with experimental data and used to provide a new insight into the nature of the soil-geogrid interaction in both cases.

RÉSUMÉ

Le comportement des géogrilles dépend principalement de l'interaction entre la géogrid et le sol avec lequel elle est en contact. La modélisation de cette interaction est difficile, particulièrement pour le comportement à l'échelle des particules de sol. Un nouvel algorithme combinant une approche par éléments finis et par éléments discrets est proposé. Les éléments finis sont utilisés pour modéliser la géogrid et les éléments discrets pour modéliser le sol en contact avec la géogrid. L'approche est appliquée à l'analyse de deux problèmes : 1) la résistance à l'arrachement de la géogrid en tension, et 2) une semelle de fondation reposant sur une couche de sable renforcée par une géogrid. Les résultats numériques sont validés par comparaison avec des données expérimentales et utilisés afin de mieux comprendre les mécanismes d'interaction entre les particules de sol et la géogrid.

1 INTRODUCTION

Continuum approaches (e.g., Finite Element and Finite Difference) are generally used for the numerical analysis of soil-structure interaction problems. The finite element method (FE) has proven to be a powerful tool to model both structural elements and the surrounding soil. Although FE can be used efficiently to model soil behavior at the macroscopic scale, the discontinuous nature of soil particles is challenging to represent. This discontinuous nature has an important role in the behavior of different soil-structure interaction systems such as soil-geogrid interlocking (McDowell et al., 2006) and soil arching in embankments (Han et al., 2011). The discrete element method (DE) proposed by Cundall and Strack (1979) is an alternative approach for the modeling of these systems. While the DE method can efficiently model soil discontinuous behavior (Lobo-Guerrero and Vallejo; 2006; Tran et al., 2012), using the DE method to model structural elements can lead to inaccurate results.

To take advantage of both FE and DE methods, the structural elements can be modeled using FE method whereas the soil matrix can be modeled using DE method. The coupling of the two methods can efficiently model the behavior of both the soil and the embedded structure. This approach has been used by several researchers to analyze certain geotechnical problems. Elmekati and Shamy (2010) used this approach to model pile installation. Dang and Meguid (2013) studied the

earth pressure distribution on tunnel linings by modeling the lining structure using FE and the surrounding soil using DE. Geotextile-reinforced embankment analysis using a coupled framework was reported by Villard et al. (2009). In this paper, a coupled Finite-Discrete element (FE-DE) framework that is capable of modeling soil-structure interaction problems at the microscopic scale level is described and used to investigate two selected geogrid-soil interaction problems involving (1) geogrid pullout test and (2) strip footing on geogrid-reinforced sand. Modeling of these problems allows for the merits of the soil-geogrid interaction to be demonstrated. In addition, stresses and displacements in the geogrid, soil stresses and particle movements are also investigated.

2 COUPLED FINITE-DISCRETE ELEMENT FRAMEWORK

The coupled FE-DE framework used in this study is implemented into an open source discrete element code YADE (Šmilauer et al., 2010) and is briefly described in the following sections.

2.1 Finite Elements

The FE analysis in the coupled framework is performed using a dynamic relaxation approach. The general equation of the dynamic method is:

$$K\mathbf{x} + cM\dot{\mathbf{x}} + M\ddot{\mathbf{x}} = \mathbf{P} \quad [1]$$

where, \mathbf{M} is the mass matrix, \mathbf{K} is the stiffness matrix, \mathbf{P} is the external force vector, \mathbf{X} represents the displacement vector and c is the damping coefficient.

In order to satisfy the convergence condition, the time step Δt_{FE} must be smaller than a maximum time step $[\Delta t_{FE}]$ determined by:

$$[\Delta t_{FE}] = \frac{2}{\sqrt{\lambda_m}} \quad [2]$$

where, λ_m is the maximum eigenvalue calculated using the element consistent tangent stiffness:

$$\lambda_m \leq \max_i \sum_{j=1}^n \frac{|K_{ij}|}{M_{ii}} \quad [3]$$

where, M_{ii} is an element of the diagonal mass matrix and K_{ij} is an element of the global tangent stiffness matrix.

2.2 Discrete Elements

The interaction between DE particles is a dynamic process based on a time-stepping algorithm with an explicit finite difference scheme. Since dynamic approach is also used in the FE analysis, it is possible to couple the two compatible approaches. In the DEM, the particle motion is determined using Newton's and Euler's equations. Energy from particle interactions is dissipated using damping coefficients. The convergence condition is satisfied when all internal and external forces are balanced. The interaction between two DE particles is determined using contact laws. The contact law used in this study is briefly described below (Figure 1a):

The interaction between the two particles A and B is represented by normal force $\bar{\mathbf{F}}_N$, tangential force $\bar{\mathbf{F}}_T$ and rolling resistance moment $\bar{\mathbf{M}}_r$. The normal and tangential contact forces are determined using the normal penetration between the two particles $\bar{\Delta}_N$ and incremental tangential displacement $\delta\bar{\Delta}_T$ such that:

$$\bar{\mathbf{F}}_N = K_N \bar{\Delta}_N, \delta\bar{\mathbf{F}}_T = -K_T \delta\bar{\Delta}_T \quad [4a, b]$$

where K_N and K_T are the normal and tangential stiffnesses at the contact. They are defined by:

$$K_N = \frac{2E_A r_A E_B r_B}{E_A r_A + E_B r_B} \quad [5]$$

and:

$$K_T = \alpha K_N \quad [6]$$

where E is the particle material modulus, r is the particle radius and α is a constant ratio.

The rolling resistance moment $\bar{\mathbf{M}}_r$ is introduced to represent the rolling restraint between the two particles A and B. $\bar{\mathbf{M}}_r$ is calculated using a rolling angular vector $\bar{\boldsymbol{\theta}}_r$ which describes the relative orientation change between the two particles by summing the angular vectors of the incremental rolling.

It is noted that both the tangential force $\bar{\mathbf{F}}_T$ and moment $\bar{\mathbf{M}}_r$ are limited by a threshold value such that:

$$\bar{\mathbf{F}}_T = \frac{\bar{\mathbf{F}}_T}{\|\bar{\mathbf{F}}_T\|} \|\bar{\mathbf{F}}_N\| \tan(\varphi_{micro}) \text{ if } \|\bar{\mathbf{F}}_T\| \geq \|\bar{\mathbf{F}}_N\| \tan(\varphi_{micro}) \quad [7]$$

and:

$$\bar{\mathbf{M}}_r = \begin{cases} K_r \bar{\boldsymbol{\theta}}_r & \text{if } K_r \|\bar{\boldsymbol{\theta}}_r\| < \|\bar{\mathbf{M}}_r\|_{lim} \\ \|\bar{\mathbf{M}}_r\|_{lim} \frac{\bar{\boldsymbol{\theta}}_r}{\|\bar{\boldsymbol{\theta}}_r\|} & \text{if } K_r \|\bar{\boldsymbol{\theta}}_r\| \geq \|\bar{\mathbf{M}}_r\|_{lim} \end{cases} \quad [8]$$

where:

$$\|\bar{\mathbf{M}}_r\|_{lim} = \eta_r \|\bar{\mathbf{F}}_N\| \frac{r_A + r_B}{2} \quad [9]$$

K_r is the rolling stiffness of the interaction computed by:

$$K_r = \beta_r \left(\frac{r_A + r_B}{2} \right)^2 K_T \quad [10]$$

where β_r is the rolling resistance coefficient and η_r is a dimensionless coefficient.

2.3 Interface Elements

Interface elements are implemented to model the interaction between the FE and DE domains. Since triangular facets are capable of reproducing complex surfaces, they are used as interface elements. A triangular facet is directly defined by the three nodes of the element located on the interface if the element has a triangular or a tetrahedron shape. In the case of quadrilateral or hexahedral elements, the contact interface is divided into four triangular facets by creating a temporary center node determined by:

$$x^{(0)} = \frac{1}{4} \sum_{i=1}^4 x^{(i)} \quad [11]$$

where $x^{(i)}$ is the coordinate of node i of the quadrilateral.

The interaction between a discrete particle and an interface element is illustrated in Figure 1b. The contact algorithm used is similar to that between DE particles: a set of potential contacts between DE particles and interface elements is first obtained through spatial sorting. The contact between a DE particle and an interface element is then determined based on the distance between the DE particle and the interface as well as the projection position of the particle center on the interface element. The normal penetration $\bar{\Delta}_N$ and the incremental tangential displacement $\delta\bar{\Delta}_T$ are determined allowing for the normal and tangential contact forces to be calculated (Eq. 4a, b). Interaction forces transmitted to FE nodes can be determined:

$$\bar{\mathbf{F}}_i = \bar{\mathbf{F}}_{contact} \cdot N_i \quad [12]$$

where $\bar{\mathbf{F}}_{contact} = \bar{\mathbf{F}}_N + \bar{\mathbf{F}}_T$ is the total contact force, N_i is the shape functions obtained using the natural coordinates of the contact point.

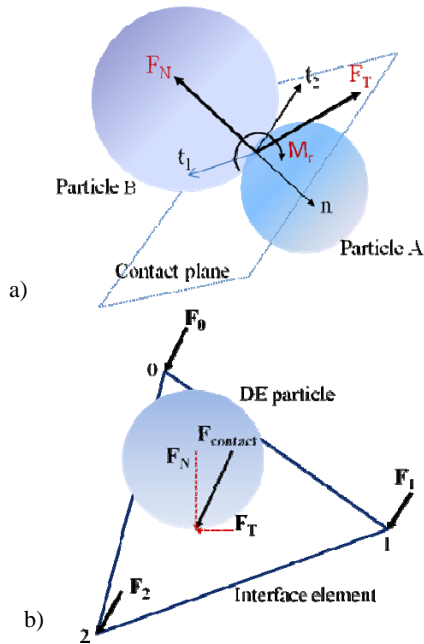


Figure 1. a) Interaction between two DE particles
 b) Forces transmitting to FE nodes through DE particle - interface element interaction

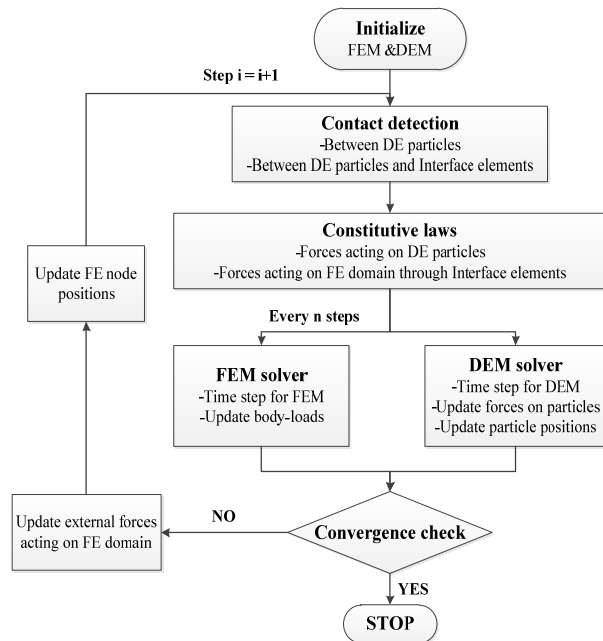


Figure 2. Flow chart for the coupled Finite - Discrete element method

It is not efficient to use a common time-step for both FE and DE models since the time-step Δt_{FE} required for FE is much larger than that for DE (Δt_{DE}). Thus, different time-steps for each domain are implemented in the coupling framework to improve the computational efficiency. The

time-step in the FE domain is selected as $\Delta t_{FE} = n\Delta t_{DE}$

where n is an integer such that $n \leq \left\lfloor \frac{\Delta t_{FE}}{\Delta t_{DE}} \right\rfloor$. This algorithm

is implemented by executing the FE solver for every n DE computations. Calculation steps in a typical cycle are illustrated in Figure 2.

3 GEOGRID PULLOUT TEST

3.1 Model Generation

In this study, an experimental pullout test performed on a geogrid type SS-1 (Alagiyawanna et al., 2001; Sugimoto and Alagiyawanna, 2003) is numerically modeled using the proposed coupled FE-DE approach. Details of the laboratory test are summarized as follows:

The soil container was reported to be 0.68 m in length, 0.3 m in width and 0.62 m in height. The front wall composed of six acrylic plates each of 0.3 m width and 0.1 m height to reduce the friction between soil and the wall. The soil used in the experiment was Silica Sand No. 5 with $D_{50} = 0.34$ mm and a peak friction angle of 29.9° ($D_r = 70\%$) as obtained from laboratory triaxial tests. A geogrid specimen (Tensar SS-1 with polypropylene material and stiffness 285.6 kN/m at a strain of 3%) of 500 mm in length and 300 mm in width was used throughout the experiments. The sand was placed in layers using raining technique and the pullout load was applied using a clamp attached to the front end of the geogrid sheet. Vertical stresses 49 kPa and 93 kPa were applied on the top and bottom of the box using air bags to prevent vertical movement of the geogrid during the test. The geogrid was pulled out at a constant rate of 1.0 mm/min and both the load and lateral movement were measured using load cells and displacement gauges, respectively.

The numerical model has been developed such that it follows the geometry and test procedure used in the actual experiment. The geogrid is modeled using FE while the soil is modeled using DE. Interface elements are used to simulate the interaction between the two domains. The biaxial SS-1 geogrid, which comprises 8 longitudinal elements and 19 transverse elements, is modeled using 8-noded brick elements with 8 integration points (Figure 3). A non-deformable clamp is introduced at one end of the geogrid. The initial distance between the front wall and the 1st transverse member is 30 mm assuring all transverse members are still in the soil domain during the test (the maximum pullout displacement is 25 mm). A linear elastic material model is used for the geogrid sheet and its properties are determined by matching the experimental load-displacement curve obtained from the conducted index tests at a medium strain of 2% (as shown in Table 1). The full geometry of the geogrid which comprises over 1300 finite elements and 20,000 interface elements is shown in Figure 3.

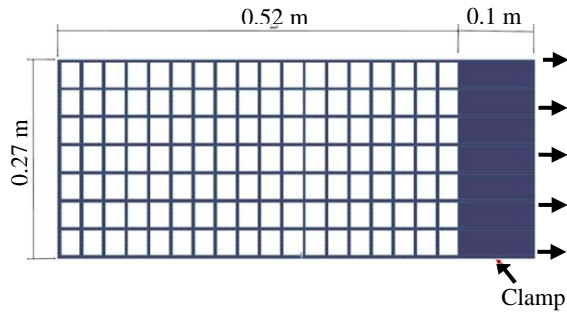


Figure 3. Geometry of the geogrid

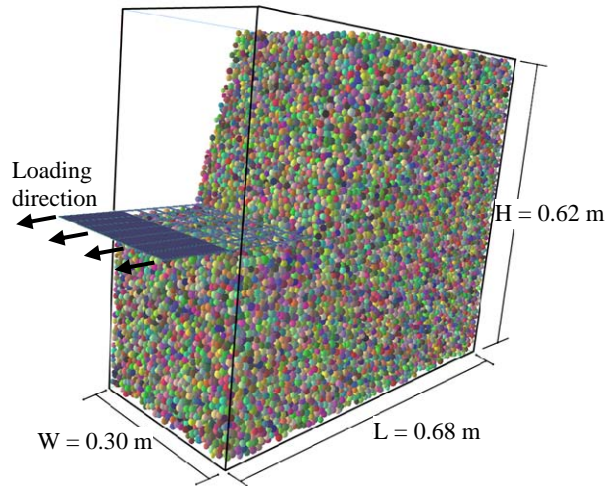


Figure 4. Initial DE specimen (partial view)

The sand used in the experiment is modeled using spherical particles. Since it is numerically prohibitive to simulate millions of particles with true sizes, particle up-scaling is necessary to reduce the number of modeled particles. In this study, the sand is modeled using discrete particles with a mean diameter of 5.1 mm (15 times the real D_{50}) and a standard deviation of 1.0 mm.

The packing algorithm (Tran et al. 2012, 2013) is used to generate the discrete soil sample with a porosity of 0.39. Particle properties are determined by matching the results of the numerical and experimental triaxial test. It is found that the most appropriate combination corresponds to a friction angle with a tangent ($\tan \phi$) of 0.54 and a particle material modulus (E) of 100 MPa. A summary of the selected parameters is given in Table 1. The 3D geometry of the final sample is partially shown in Figure 4.

3.2 Pullout Test Model

After the final specimen is formed, the input parameters (Table 1) are then assigned to the discrete particles and the finite elements. No friction is used for the interaction between the particles and the box (smooth rigid) to reduce the boundary effects. A parametric study was conducted to examine the effect of the contact parameters between the discrete particles and interface elements on the calculated response of the pullout model.

Results indicated that the stiffnesses at the interface do not have a significant effect on the pullout test results. Therefore, the stiffnesses of the interface have been assigned the same values as that of the discrete particles. On the other hand, the coefficient of friction between the discrete particles and interfaces was found to affect the overall response of the soil-geogrid system. In this study, the particle-interface coefficient of friction is determined to be 0.95 based on matching the numerical results with experimental data.

Table 1. Input parameters (pullout test problem)

Elements	Parameter	Value
Discrete particles	Density (kg/m^3)	2640
	Material modulus E (MPa)	100
	Ratio K_T/K_N	0.1
	Coefficient of friction	0.54
	β_r	0.05
	Damping coefficient	0.2
Finite elements	Young modulus E (MPa)	2.8E+3
	Poisson's ratio ν	0.3
Interface elements	Material modulus E (MPa)	100
	Ratio K_T/K_N	0.1
	Coefficient of friction	0.95

Following the above step, the geogrid is allowed to freely deform and the two vertical stresses (σ_v) 49kPa and 93kPa are applied above and below the soil sample. The vertical stress is kept constant during the test using a stress control mechanism. The pullout procedure is numerically performed using a displacement control approach: lateral displacements were applied to the clamp in 12 steps. In each step, the clamp was forced to move with a same rate of the experiment (in simulation time scheme) until an increase of displacement of 2.5mm was reached. The clamp movement was then stopped until convergence conditions are satisfied in both the DE and FE domains. Additional frontal displacements were applied in subsequent steps and the procedure continued until the frontal displacement U_x reached 25 mm.

3.3 Simulation Results

The relationship between the pullout force and the frontal displacement is shown in Figure 5 as obtained from both the experimental and numerical models. The numerical results generally agreed with the experimental data except for smaller pullout forces that are calculated for frontal displacements less than 7 mm. This is expected given the limited number of discrete particles used to represent the backfill soil resulting in underestimating the interaction between particles and interfaces particularly at the early stages of the test. The pullout force at a given frontal displacement slightly increased as the vertical stress changes from 49 kPa to 93 kPa. Sugimoto and Alagiyawanna (2003) observed a small slippage of the

geogrid at both stress levels leading to marginal difference in pullout resistance. Figure 6 shows the displacement distributions along the geogrid. It can be seen that geogrid displacements decreased with distance from the face. For all examined frontal displacements the geogrid displacement (U_x) occurred within a limited region from the front side to about the middle of the geogrid. Very small displacements were calculated outside this region. Figure 6 also confirms the agreement between the measured and calculated displacement using the proposed framework.

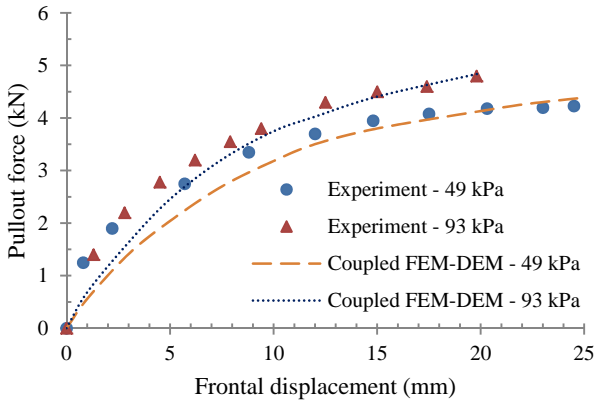


Figure 5. Pullout response of the geogrid

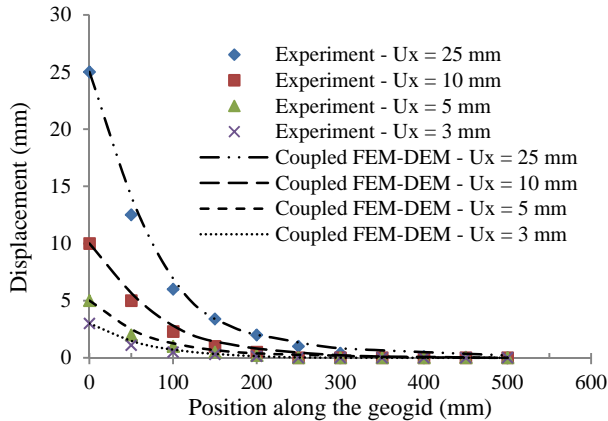


Figure 6. Horizontal Displacement along the geogrid ($\sigma_v = 49$ kPa)

The tensile force distributions in the longitudinal members for different frontal displacements are illustrated in Figure 7. At a given location along the geogrid, the average tensile force (P_{xx}) in all longitudinal members was found to increase with the increase in frontal displacements. For the investigated range of frontal displacements, the force P_{xx} was large near the front end and rapidly decreased towards the middle of the geogrid. Beyond the middle zone, P_{xx} became negligible due to the insignificant displacement of the geogrid experienced by the rest of the geogrid.

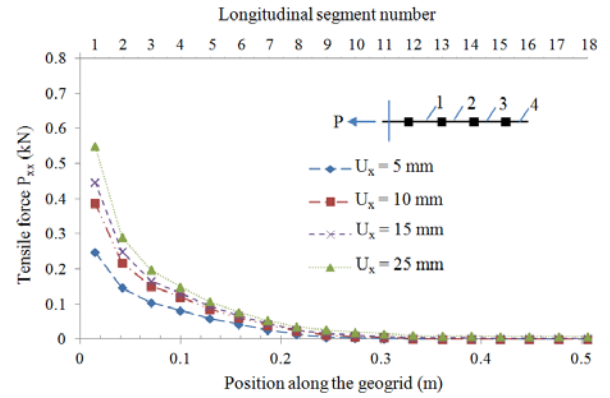


Figure 7. Average tensile force P_{xx} in the longitudinal members ($\sigma_v = 49$ kPa)

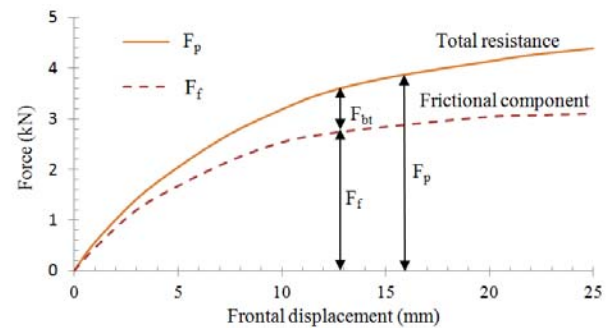


Figure 8. Components of the pullout resistance ($\sigma_v = 49$ kPa)

The geogrid comprises longitudinal and transverse members as well as joints connecting these members. Each of these components contributes to the total pullout force. Since the resistance of the joints in this study is numerically included in the frictional resistance of the geogrid, the total pullout resistance F_p can be written as:

$$F_p = F_f + F_{bt} \quad [13]$$

Where F_f is the frictional resistance on the geogrid surface, F_{bt} is the bearing resistance of the transverse members.

Contribution of each component to the total pullout resistance is shown in Figure 8. It can be seen that the contribution of the bearing resistance is less than that of the frictional resistance for all considered frontal displacements leading to the frictional component (F_f) dominating the pullout resistance F_p . However, the rate of increase in F_f became very small when the frontal displacements (U_x) reached about 18 mm as slippage of the geogrid started to develop and most of the shear forces between the particles and interfaces reached their maximum value. The bearing resistance of the transverse elements, on the other hand, shows an increase in value for all examined frontal displacements.

Figure 9 shows the displacement field across the soil domain at a frontal displacement of 10 mm. It can be seen that most of the soil movement developed near the front face of the box leading to soil densification in that area. Soil movement gradually decreased and became

negligible around the middle of the geogrid as there is no significant geogrid displacement in this area. Soil in the vicinity of the geogrid tends to move horizontally towards the front face whereas near the front face soil tends to move vertically away from the geogrid. These observations agree well with the results of the X-ray radiographs reported by Alagiyawanna et al. (2001).

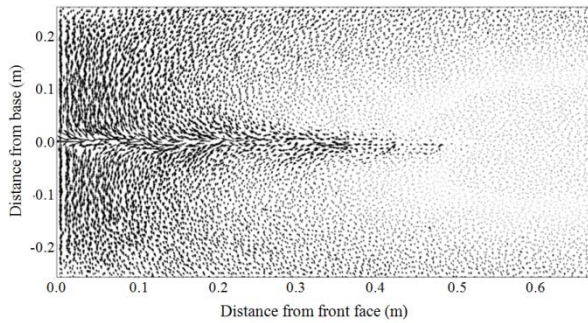


Figure 9. Displacement field of the soil domain at $U_x = 10$ mm and $\sigma_v = 49$ kPa

4 STRIP FOOTING ON GEOGRID-REINFORCED SAND

4.1 Model Generation

Numerical simulation of strip footing on geogrid-reinforced sand using the proposed coupled FE-DE model is conducted following the experiment reported by Das et al. (1994). In the experiment, the soil container was reported to be 1.1m in length, 0.3m in width and 0.9m in height. The walls were polished to reduce the friction between the soil and the wall. The strip foundation had a width of 76 mm (noted as B) and a length of 300 mm. A rough condition at the base of the foundation was generated by cementing a thin layer of sand at the contact surface. The soil used in the experiment was medium-grained silica sand with $D_{50} = 0.51$ mm, average dry unit weight of 17.14 kN/m³ and a peak friction angle of 41° (at $D_r = 70\%$) obtained from laboratory direct shear tests. Biaxial geogrids (Tensar SS-0 with PP/HDPE copolymer material and tensile modulus of 182 kN/m at 2% strain) of 760 mm in length and 300mm in width were used in the experiment. The top geogrid layer was installed at a depth 25 mm (0.33B) below the foundation base. The number of geogrid layers installed in soil was varied and the distance between two adjacent layers was 25 mm (0.33B). The sand was placed in layers of 25mm using raining technique. The geogrid layers were placed at predetermined locations. The model foundation was then placed on the soil surface and vertical loading was applied using a hydraulic jack.

Up to two geogrid layers are considered in this study. Interface elements are used to simulate the interaction between the geogrid (modeled using FE) and the soil (modeled using DE). Eight-node brick elements are used to model the geogrid consisting of 11 longitudinal elements and 21 transverse elements. A linear elastic material model is used for the geogrid sheet and its

properties are shown in Table 2. The sand is modeled using discrete spherical particles with a mean diameter of 10.2 mm (20 times the real D_{50}) and a standard deviation of 2.0 mm. Soil samples are generated using the gravitational approach proposed by Tran et al. (2012, 2013) to represent the actual soil placement in layers under gravity. Particle properties determined by matching the results of the numerical and experimental direct shear test are shown in Table 2.

Table 2. Input parameters (strip footing problem)

Elements	Parameter	Value
Discrete particles	Density (kg/m ³)	2650
	Material modulus E (MPa)	38
	Ratio K_T/K_N	0.25
	Coefficient of friction	0.68
	β_r	0.01
	Damping coefficient	0.2
Finite elements	Young modulus E (MPa)	1.4E+3
	Poisson's ratio ν	0.3
Interface elements	Material modulus E (MPa)	38
	Ratio K_T/K_N	0.25
	Coefficient of friction	0.42

After the final specimen is formed, the strip footing (76 mm x 300 mm, Figure 10) is numerically generated and initially placed at the surface of the soil layer. The input parameters are then assigned to the discrete particles and the finite elements. The stiffnesses of the interface elements are assigned the same values as the DE particles as discussed in previous parts. A particle-interface coefficient of friction of 0.42 is determined for the simulation to match the experimental results. The geogrids are then allowed to freely deform and pressure at the foundation base is applied in small increments using a stress control mechanism. Each load increment is kept constant until convergence conditions are satisfied in both the DE and FE domains. The foundation pressure is then increased for the next stage.

4.2 Simulation Results

The coupled FE-DE simulation results are first compared with the experimental data. Figure 11 shows the relationship between the foundation pressure and settlement for three cases: no reinforcement ($N = 0$), one geogrid layer ($N = 1$) and two geogrid layers ($N = 2$). It can be seen that the numerical results agreed well with the experimental data for all cases. The ultimate bearing capacity calculated by Das et al. (1994) is consistent with the numerical results. This confirms the agreement between the experiment and numerical simulations using the proposed numerical framework.

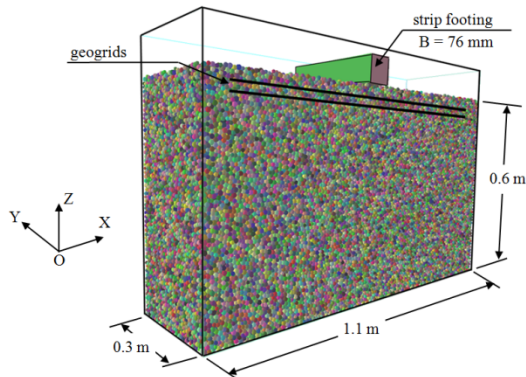


Figure 10. Initial geometry of the geogrid reinforced foundation

The deformed shapes of the geogrid layers for a foundation pressure $q = 125$ kPa are shown in Figure 12. The vertical displacement of the geogrid for one reinforcement layer ($N = 1$) is shown in Figure 12a whereas the case of two geogrid layers ($N = 2$) is shown in Figure 12b. It can be seen that the vertical displacement of the geogrid for $N = 1$ is generally larger than that for $N = 2$. In addition, the vertical displacement of the upper geogrid sheet is larger than that of the lower one. In both cases, the deformations of the geogrids occurred mainly in a region below the foundation and very small deformations were observed outside that region.

The maximum calculated vertical displacements and tensile stresses in the geogrid for different footing pressures are shown in Figure 13. It is observed that for a given pressure, the vertical displacements and tensile stresses in the geogrid were larger for $N = 1$ than for $N = 2$. It is also noted from Figure 13a and 13b that the deformation and tensile stresses of the upper geogrid layer were generally larger than the lower one for $N = 2$.

The distribution of vertical stresses with depth beneath the center of the footing is shown in Figure 14. An increase in the vertical stress in the zone above the geogrids can be seen. However, there was no significant change in the vertical stress beyond a depth of 1.2B below the geogrids.

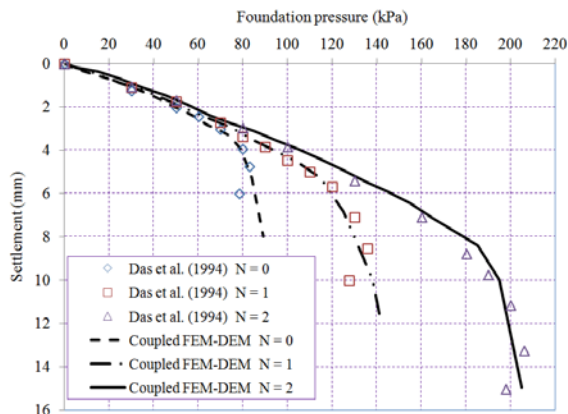


Figure 11. Load-settlement curves

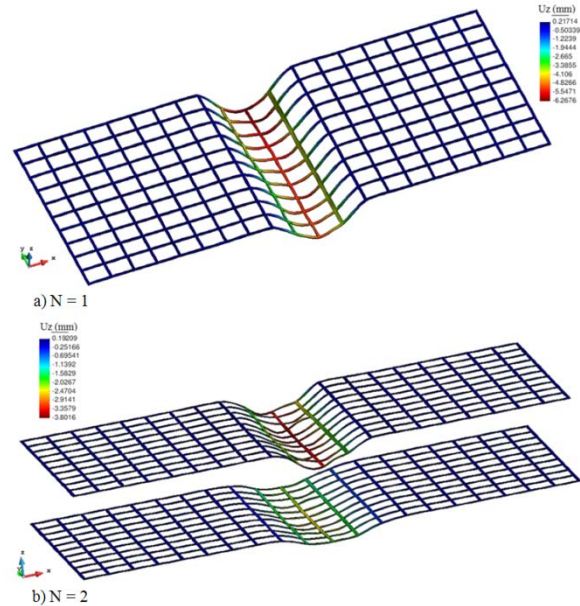


Figure 12. Geogrid vertical displacement at foundation pressure $q = 125$ kPa. a) one geogrid layer and b) two geogrid layers

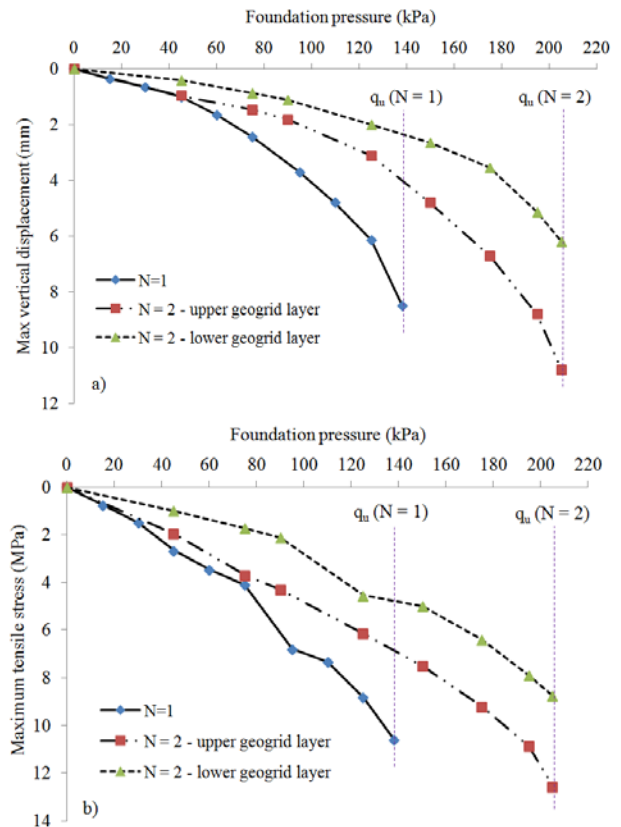


Figure 13. a) Maximum vertical displacements of geogrids
b) Maximum tensile stresses of geogrids

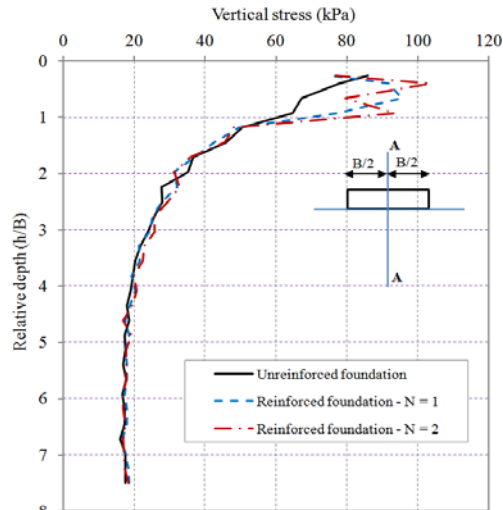


Figure 14. Vertical stress distributions beneath the strip foundation (cross section A-A)

5 SUMMARY AND CONCLUSIONS

This study investigated the numerical modeling of soil-geogrid interaction problems using a coupled FE-DE framework. The soil was modeled using DE while the geogrid was modeled using FE. The interaction between the DE and FE domains was ensured by using interface elements. The developed framework was used to investigate two geotechnical problems: geogrid pullout test and strip footing on geogrid-reinforced sand.

In the geogrid pullout simulation, most of the geogrid stresses and displacements occurred near the front side of the box with rapid decrease with distance and reached very small values around the middle of the geogrid. For the investigated geogrid and soil conditions, the contribution of the frictional resistance to the total pullout resistance was found to be larger than the bearing resistance. The contribution of the bearing resistance to the overall capacity increased as the geogrid displacement increased. The soil movement distribution within the soil domain agreed with experimental observations.

In the strip footing simulation, the numerical modeling of the geogrid reinforced strip foundation provided a very good agreement with the experimental results. Geogrid deformations and tensile stresses for $N = 1$ were larger than those for $N = 2$. When two layers of geogrid were used, the upper layer was subjected to larger deformations and tensile stresses than the lower layer. The use of geogrid reinforcement also resulted in an increase in the vertical stresses in the soil.

Finally, the proposed coupled FE-DE method is proven to be effective in capturing soil-geogrid interactions and to analyze the responses of both the geogrid and the surrounding backfill material.

ACKNOWLEDGEMENTS

This research is supported by a research grant from the Natural Sciences and Engineering Research Council of Canada (NSERC). The financial support provided by

McGill Engineering Doctoral Award (MEDA) to the first author is greatly appreciated.

REFERENCES

- Alagiyawanna, A.M.N., Sugimoto, M., Sato, S., Toyota, H., 2001. Influence of longitudinal and transverse members on geogrid pullout behaviour during deformation, *Geotextiles and Geomembranes*, 19 (8), 483–507.
- Cundall, P.A., and Strack O.D.L. 1979. A discrete numerical model for granular assemblies, *Géotechnique*, 29(1): 47-65.
- Dang, H.K., and Meguid, M.A. 2013. An efficient finite-discrete element method for quasi-static nonlinear soil-structure interaction problems, *International Journal for Numerical and Analytical Methods in Geomechanics*, 37(2), 130-149.
- Das, B.M., Shin, E.C., and Omar, M.T. 1994. The bearing capacity of surface strip foundations on geogrid-reinforced sand and clay—a comparative study, *Geotechnical and Geological Engineering*, 12(1), 1-14.
- Elmekati, A., and Shamy, U.E. 2010. A practical co-simulation approach for multiscale analysis of geotechnical systems, *Computers and Geotechnics*, 37(4), 494–503.
- Han, J., Bhandari, A., and Wang, F. 2011. DEM Analysis of Stresses and Deformations of Geogrid-Reinforced Embankments over Piles, *International Journal of Geomechanics*, 12(4), 340–350.
- Lobo-Guerrero, S., and Vallejo, L.E. 2006. Discrete element method analysis of railtrack ballast degradation during cyclic loading, *Granular Matter*, 8(3), 195-204.
- McDowell, G.R., Harireche, O., Konietzky, H., Brown, S.F., Thom, N.H., 2006. Discrete element modelling of geogrid-reinforced aggregates, *Proceedings of the ICE - Geotechnical Engineering*, 159 (1), 35-48.
- Šmilauer, V., Catalano, E., Chareyre, B., Dorofeenko, S., Duriez, J., Gladky, A., Kozicki, J., Modenese, C., Scholtès, L., Sibille, L., Stránský, J., and Thoeni, K. 2010. Yade Documentation, *The Yade Project, 2010*. (<http://yade-dem.org/doc/>).
- Sugimoto, M., Alagiyawanna, A.M.N., Kadoguchi, K., 2001. Influence of rigid and flexible face on geogrid pullout tests, *Geotextiles and Geomembranes*, 19 (5), 257–277.
- Tran, V.D.H., Meguid, M.A., and Chouinard, L.E. 2012. Discrete Element and Experimental Investigations of the Earth Pressure Distribution on Cylindrical Shafts, *International Journal of Geomechanics* (online).
- Tran, V.D.H., Meguid, M.A., and Chouinard, L.E. 2013. A Finite-Discrete Element Framework for the 3D Modeling of Geogrid-Soil Interaction under Pullout Loading Conditions, *Geotextiles and Geomembranes*, 37, 1-9.
- Villard, P., Chevalier, B., Hello, B.L., and Combe, G. 2009. Coupling between finite and discrete element methods for the modelling of earth structures reinforced by geosynthetic, *Computers and Geotechnics*, 36 (5), 709–717.